UNIVERSITY of CALIFORNIA

SANTA CRUZ

ON THE DETECTION OF PLANETARY SPIN IN TRANSIT DATA

A thesis submitted in partial satisfaction of the

requirements for the degree of

BACHELOR OF SCIENCE

in

EARTH SCIENCE (PLANETARY SCIENCE)

by

Reid Sherman

June 2012

The thesis of Reid Sherman is approved by:

Gregory Laughlin
Advisor

Abstract

On the Detection of Planetary Spin in Transit Data

by

Reid Sherman

Although axial rotation of a planet detected in transit is not directly observable, the behavior of a natural satellite may indirectly characterize the spin rate. Three systems – two based on planets found by the *Kepler* Spacecraft and the Sun-Earth-Moon system – are modeled with a three-body Bulirsch-Stoer style numerical integrator. Modulated by two variables: the moon's semi-major axis, a_m; and the planet's spin rate, s, I demonstrate how synthetic light curve data encodes the effect of planetary spin on photometry obtained during transit over a five year time span. I find that for reasonable photometric precision, planetary spin only generates a noticable effect as moons approach a quarter of the Hill radius, for planetary densities < 6 g/cc. The light curves are compared using the moon's independent transit duration, t'_m, over the entire five year time span. As t'_m shows no direct relationship to the planetary spin rate, quantification of the planetary spin rate from the exomoon's signal is indeterminable.

Chapter 1

Introduction

The sheer amount of known transiting planetary candidates begs the question as to whether a transiting natural satellite, or *exomoon*, is currently detectable. In effect, an informal "space-race" to detect the first exomoon pervades extrasolar-system research. The orbital motion of a natural satellite offers an indirect route to infer certain characteristics of its host planet. This thesis provides an order-of-magnitude approach to constrain planetary spin using a natural satellite. More specifically, I investigate if the transit signal of an exomoon can be used to indirectly constrain the axial spin rate of the exoplanet. Lacking direct exomoon detection data, the core of this project is a sophisticated three-body integration routine; initially designed to model the long-term "tidal, spin, and dynamical evolution of a many-body system" (Mardling and Lin, 2002). To mimick to the current resolution of space telescope transit data, I modify the computer program to generate long-cadence (30 min/measurement) transit data over a five year time span. Input parameters for the program are taken from the catalog of *Kepler* planetary

candidates as tabulated by Batalha et al. (2012), with a particular emphasis for those with favorable moon-hosting characteristics. These systems are input into the computer routine and their transit signals are analyzed in an attempt to reverse-engineer the planetary rotation rate. Ultimately, a caveat of this project is exomoons remain elusive to current exoplanet detection techniques. The multitude of theories behind exomoon detection, e.g. the techniques described in Barnes and O'Brien (2002), Simon et al. (2010), Kipping (2011), Kipping (2012), and many others may bring a transiting exomoon to fruition in the foreseeable future. A few decades ago nobody could have predicted the power of the transit technique to detect exoplanets – the near future may harbor an explosion of exomoon discovery using similar, yet refined methods.

In effect, the objectives of this study are: i) Extract moon-favorable orbital configurations from Kepler planetary candidate data; ii) generate light curves with a spinning planet and a moon at a variable semi-major axis within reason; and iii) interpret the relationship between planetary spin and the moon's transit signal and discuss the feasibility of this method.

1.1 Planetary Candidate Selection Process

Over 2300 *Kepler* planetary candidates are catalogued in Batalha et al. (2012) to $< 15\%$ false alarm probability. Transit depths range from 0.002% (KOI 5.02) to nearly 9% (KOI 998.01), depending on their respective orbital characteristics, radius, and spectral properties. Considering Earth's moon, it is possible for a natural satellite radius to be 30% of its primary. On the other hand, for gas giants the satellite-planet radii ratio drops off considerably, e.g., Europa's radius is merely 2% of Jupiter's. Although *Kepler* is tuned to pick up extremely small light

flux discrepancies, exomoon transits likely occur simultaneously with their primary; meaning their signal may be completely dwarfed. For this experiment, only Earth or super-Earth radii planetary candidates are investigated. To a first order approximation, planetary mass and radius are correlated. The goal of this section is to approximate planetary mass as a function of the known planetary radius for $\approx R_{\oplus}$ sized candidates. From the planetary mass, one can constrain r_H, the Hill radius, within which natural satellites are theoretically stable.

Assuming the planetary period and star mass, M_s, is known, the semi-major axis of the primary body is then calculable using Kepler's Third Law:

$$GM_s = n^2 a^3 \qquad M_p \ll M_s$$

$$a = (GM_s/n^2)^{1/3} \tag{1.1}$$

where n is the mean motion (2π/period) and a represents the semi-major axis, the log (g) value from Batalha et al. (2012):

$$GM_s = 10^{log(g)} R_s^2$$

combine with (1.1)

$$a = (10^{log(g)} R_s^2/n^2)^{1/3} \tag{1.2}$$

Although the planetary density is calculable in certain special cases, the transit method is incapable of directly measuring the transiting planet's mass. Therefore, a constant density scaling relationship for terrestrial-like bodies ($R_p < 3R_{\oplus}$) is used to approximate mass as a function of radius. Valencia et al. (2006) states:

$$R_p \, \alpha \, M_p^{0.267-0.272}$$

$$M_p \, \alpha \, R_p^{1/0.267-1/0.272} \approx R_p^{3.71} \tag{1.3}$$

I adopt the mean of the value range (1/0.267 to 1/0.272), 3.71. The values for the planetary radius, R_p, are taken from Batalha et al. (2012). The Hill radius, r_H, is the semi-major axis where the gravitational pull from the planet equates the tidal gravity of the star. Given by the equation from Murray and Dermott (1999), in the limit $M_{moon} \ll M_p$:

$$r_H = a_p(M_p/3M_s)^{1/3}$$

combine with (1.1), (1.2), and (1.3):

$$r_H \approx (GR_p^{3.71}/(3n^2))^{1/3} \tag{1.4}$$

In units of Earth radii.

Whereas retrograde satellites are theoretically capable of orbiting stably near the Hill sphere boundary, prograde satellites find themselves on unstable trajectories well inside r_H; Domingos et al. (2006) places the maximal semi-major axis for prograde satellites at $\approx r_H/2$.

A minimum value is also required to define the entire range of theoretically plausable semi-major axes. The Roche limit, r_L, provides a minimum distance at which tidal forces will tear an orbiting satellite apart. For fluid-like bodies, Weidner and Horne (2010) defines r_L as:

$$r_L = 2.44R_p(\frac{\rho_p}{\rho_m})^{1/3} \tag{1.5}$$

Simulations are based on known planetary candidate orbital configurations from the latest Kepler data in Batalha et al. (2012). Candidates at extremely small semi-major axes (< 0.5AU) are filtered out on the basis most of these objects are likely tidally locked to the star. Candidates are also discarded if their radius exceeds $3R_\oplus$, because the mass scaling relationship in Valencia et al. (2006) becomes unrealistic for extremely large planets. As a result, two candidates are

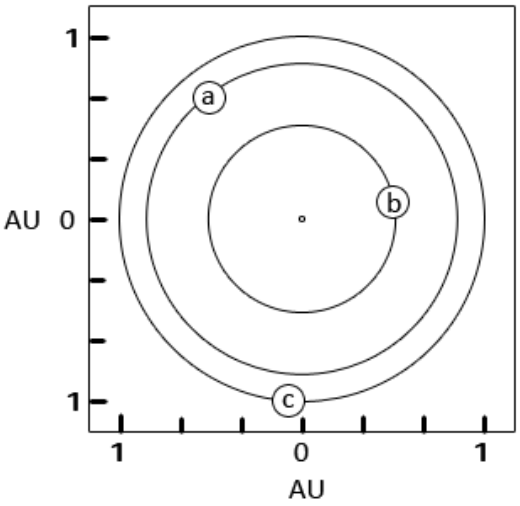

Figure 1.1: With a star at the origin (0,0), scale representation of the semi-major axis of planets a, b, and c; Keper-22b, KOI 1503.01, and the Control planet, respectively.

observed to best match the aforementioned criteria: KOI 1503.01; and KOI 87.01, better known as Kepler-22b from Borucki et al. (2012). Recall at most 15% of the 2300 planetary candidates may be false positives, so proper vetting must be performed on KOI 1503.01 before it should be considered confirmed and receive a "Kepler-" prefix. An additional control case based on the Sun-Earth-Moon system is used for comparative analysis. Figure 1.1 schematically illustrates the semi-major axes of the three configurations.

1.2 Modelling Planetary Rotation

The numerical integration routine, explained in detail in the Methods chapter, was originally designed for tidal evolution of hot Jupiters over extremely long (G.y.) timescales (see Mardling

and Lin (2002)). A sophisticated range of parameters are thus required to describe the simulated planet and satellite.

The planets are modelled as spinning fluid-like spheres which experience a 'flattening' effect wherein the equator is stretched outward. Additionally, the gravitational influence from an orbiting satellite may invoke a periodic effect on the primary's equatorial bulge. A moon-induced tidal bulge, however, is not easily calculable as it depends on both the orbital configuration as well as the internal structure of the two bodies. If the mass of the planet and the period of the moon are observable, then the semi-major axis of the moon is calculable using Kepler's Third Law. Unfortunately, even with the moon's semi-major axis, the tide raising potential is only calculable if the moon's mass is also known. If an exomoon is detected in transit, it will surely help constrain the mass of the exoplanet using Kepler's third law, however, the moon's mass is not directly observable.

The numerical integrator, explained in detail in Section 2.1, allows the planet to spin arbitrarily fast without planetary breakup. Thus, one must be careful to constrain the spin rate to a "realistic" value. To relate the density at which the planet will disintegrate due to its spin freqency, f, equate the escape velocity to the equatorial rotational velocity:

$$v_{esc} = (\text{circumference})(\text{frequency})$$

$$\sqrt{\frac{2GM}{R}} = (2\pi R)(f)$$

Rewrite (M)ass in terms of (R)adius and the planetary bulk density, ρ_p:

$$f \approx \sqrt{\frac{2}{3\pi} G\rho_p} \tag{1.6}$$

Applying (1.6), a 'rocky' planet of $\rho_p = 5.5g/cc$ would disintegrate if the length of a day were

≈ 7.8 hours. Rearrange (1.6) to approximate the minimum planetary density as a function of f:

$$\rho_p = f^2 \frac{3\pi}{2G} \tag{1.7}$$

It is no coincidence the maximum rotation frequency used in this thesis is $1/3600\ s^{-1}$, which equates a minimal bulk planetary density of ≈ 5.5 g/cc, approximately Earth's bulk density.

Chapter 2

Methods

2.1 Numerical Integration

There exists no closed analytical solution to the three-body problem, so a computer routine must step through simulation time calculating the position and velocity three-vectors for each body. This process balances computing time with precision - the smaller the steps the closer the output converges to the "true" value. However, more computing time and computer memory are required for smaller timesteps. Thus, a clever technique to vary the size of each step depending on the state of the program is built into the integration routine. To model the planet-moon-star system, a three-body numerical integration routine, initially developed by Mardling and Lin (2002), is utilized to calculate the six orbital elements for the three bodies over a synthetic five-year time span. The Bulirsch-Stoer algorithm is the mathematical engine used to balance precision with time and solve the ordinary differential equations in the computer routine. (Press

et al., 1986, p.724) describes the Bulirsch-Stoer method as "the best known way to obtain high-accuracy solutions to ordinary differential equations with minimal computational effort." To maintain computational precision, the timestepping method depends on the orbital separation of the innermost bodies, cubed. During perigee and during transit, the interval per timestep slows to a crawl. The nature of the Bulirsch-Stoer algorithm makes it nontrivial to measure light intensity with the same cadence as *Kepler*. Thus, when creating simulated *Kepler* light curve data, the measurement frequency is 30 +/- 0.01 minutes/measurement. For the planet and moon, the moment of inertia, Love numbers, obliquities, Q-values, spin frequencies, and radii were input to the integration. The simulated star is treated as a point mass with orbital characteristics (mass, semi-major axis) from Batalha et al. (2012). Simulated transits are recorded at alignment between the planet and/or moon with the star with respect to the 'y' axis on Figure 2.2. Put another way, synthetic flux data is collected when the planet, moon, or both transit the star. The resultant light curve, lc, as a function of time, t, is:

$$lc(t) = \begin{cases} (i)\ 1 & \text{Normalized Star Light Flux} \\ (ii)\ 1-(R_p/R_s)^2 & \text{During Planet Transit} \\ (iii)\ 1-(R_p/R_s)^2-(R_m/R_s)^2 & \text{During Planet and Moon Transit} \\ (iv)\ 1-(R_m/R_s)^2 & \text{During Moon Transit } (t'_m) \end{cases} \tag{2.1}$$

Where R_p, R_s, R_m, are the radii of the planet, star, and moon, respectively. Figure 2.1 schematically demonstrates the three transit phases. In systems with a longer independent moon transit duration the moon's signal is more easily detectable. I posit phase (iv) is important for moon detection and may be correlated to the planetary spin rate. The overall duration of independent moon transit over the five year integration is termed t'_m.

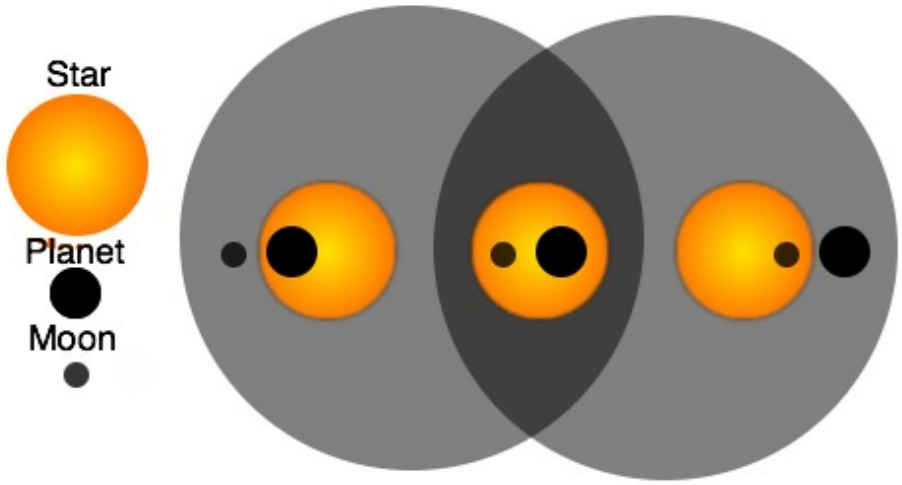

Figure 2.1: Schematic of three transit phases; from left to right, Planet Transit (*ii*), Planet and Moon Transit (*iii*), Moon Transit (*iv*). Not to scale for the systems used in this thesis.

2.2 Input Parameters

The timescale per light curve simulation is fixed to five years, roughly the length of the *Kepler* mission. Over 80,000 timesteps per simulation are performed over the virtual five-year time span – roughly 48 +/- 0.5 measurements per earth day. The orbital characteristics of the star and planet are shown in Table 3.1, taken from Batalha et al. (2012). Moons which achieve non-Keplerian, eccentricity ≥ 1, unbound orbits are discarded to maintain the five year simulation run time across every integration.

The simulated exoplanets and moons are modelled similarly to Earth. Relatively large moons tend to follow prograde orbits in our solar system, so retrograde satellites are not investigated. As mentioned earlier, mass is not directly calculable from transit data, so a "terrestrial-like" scaling argument based on radius is invoked. The moon mass is set to 1% of the planet's, roughly

the Earth-Moon mass ratio. To balance realism with detection probability, the maximal semi-major axis of each simulated moon, even in the control case, is set to $r_H/2$. This value is set as the maximum stable semi-major axis for a natural satellite established by Domingos et al. (2006). Realistically, not all moons exist at the fringe of the Hill sphere, so the semi-major axis varies incrementally at $1/2^n$ chunks, e.g., $r_H/4, r_H/8, r_H/16$, etc, were also investigated for every system.

The simulated satellites are set to synchronously orbit about their host planet, regardless of semi-major axis. Pertaining to the planetary interior structure, there are no asteroseismology measurements even for planets in our own solar system. Even Q measurements of other planets in our own solar system have significant error margins, so all simulations use high Q values (10^3) to maintain bound moon orbits. This assumption broadens the range of possible moon semi-major axes, since low Q planets tend to dissipate energy poorly, their orbits decay significantly quicker. The tidal Love number, k for the primary is set equal to Earth's k of ≈ 0.4 in every case. Logically, the larger the ratio $R_m : R_p$ the higher the probability of a moon detection, so the method of analyzing the light curves is resistant to this effect by keeping the ratio constant in every configuration; for all systems, $R_m = R_p/10$. The numerical values are displayed in Tables 3.1 and 3.2 in the Results section.

Figure 2.2 demonstrates the scale of the moon's semi-major axis to the stellar radius for every configuration. Moons which fringe r_H are more likely to transit separately from the primary. However, these moons also experience less tidal torques from the primary, so in order to gauge the effect of spin on transit data, the moon's semi-major axis varies by $r_H/2^n$, from $0 \geq n > 6$. A more in-depth analysis of spin should test moons at any arbitrary area between r_H and r_L,

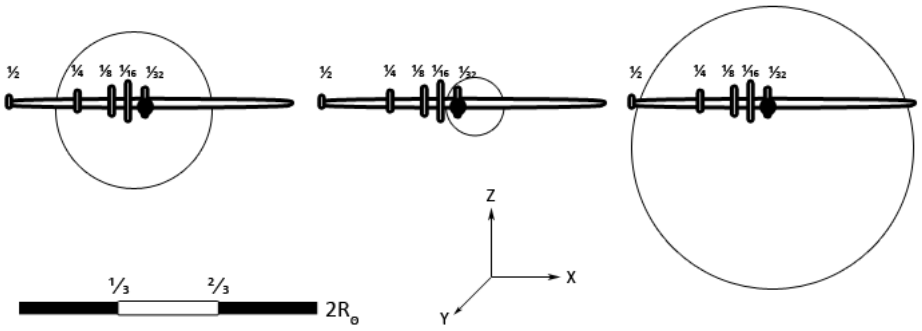

Figure 2.2: Schematic of the three orbital configurations used to test the effect of planetary spin: from left to right, Kepler-22, KOI 1503, and Control. The large circle represents the star, to scale. whereas the long axis of the thin ellipse represents $r_H/2$, also to scale. The tick marks represent the other semi-major axes tested, at $r_H/2^n$ intervals, $0 \geq n > 6$. Planetary radius not to scale, moon not shown, 1/64 tick not shown.

in both retro- and prograde orbits.

Chapter 3

Results

Insanity: doing the same thing over and over again and expecting different results.

– Albert Einstein

Designation	Planetary Radius	Period	Semi-Major Axis	log(g) (Star)	Mass	r_H
Kepler-22b (a)	2.10 $R_\oplus$	289.86 Days	0.85 AU	4.50	15 $M_\oplus$	0.019 AU
1503.01 (b)	3.36 $R_\oplus$	150.24 Days	0.511 AU	4.66	90 $M_\oplus$	0.091 AU
Control (c)	1.00 $R_\oplus$	365.25 Days	1.000 AU	3.33	1. $M_\oplus$	0.010 AU

Table 3.1: System parameters. Scaled mass based on terrestrial-like planetary mass scaling relationship from Valencia et al. (2006) $M_p \ \alpha \ R_p^{3.71}$

System	Parameter	Value	Units
All Systems	Planet Moment of Inertia (I/MR^2)	0.3308	n/a
	Planet Inclination (i)	0	Deg.
	Planet Argument of Periapse (ω)	0	Deg.
	Planet Longitude to Line of Nodes (Ω)	0	Deg.
	Planet Q Value	10^3	n/a
	Planet Obliquity	0	Deg.
	Planet Love Number (k)	0.4	n/a
	Moon Moment of Inertia (I/MR^2)	0.39	n/a
	Moon Argument of Periapse (ω)	0	Deg.
	Moon Longitude to Line of Nodes (Ω)	0	Deg.
	Moon Q Value	10^3	n/a
	Moon Love Number (k)	0.4	n/a
	Star Eccentricity	0	n/a
	True Anomaly, All Objects	0	Deg.
Kepler-22 (a)	Planet Mass	15	$M_\oplus$
	Planet Radius	2.10	$R_\oplus$
	Moon Semi-Major Axis (Max, Min)	(0.00950, 0.00015)	AU
	Moon Mass	0.15	$M_\oplus$
	Moon Radius	0.21	$R_\oplus$
	Star Semi-Major Axis	0.805	AU
	Star Mass	1.07	$M_\odot$
	Star Radius	0.85	$R_\odot$
	Valid Trial Runs	49	n/a
KOI 1503 (b)	Planet Mass	90	$M_\oplus$
	Planet Radius	3.36	$R_\oplus$
	Moon Semi-Major Axis (Max, Min)	(0.00455, 0.00007)	AU
	Moon Mass	0.90	$M_\oplus$
	Moon Radius	0.336	$R_\oplus$
	Star Semi-Major Axis	0.511	AU
	Star Mass	0.91	$M_\odot$
	Star Radius	0.61	$R_\odot$
	Valid Trial Runs	33	n/a
Control (c)	Planet Mass	1	$M_\oplus$
	Planet Radius	1	$R_\oplus$
	Moon Semi-Major Axis (Max, Min)	(0.00260, 0.00041)	AU
	Moon Mass	0.01	$M_\oplus$
	Moon Radius	0.1	$R_\oplus$
	Star Semi-Major Axis	1	AU
	Star Mass	1	$M_\odot$
	Star Radius	1	$R_\odot$
	Valid Trial Runs	43	n/a

Table 3.2: Comprehensive list of important orbital parameters for all three systems. Data resulting from trials in which the moon's final eccentricity ≥ 1 were discarded.

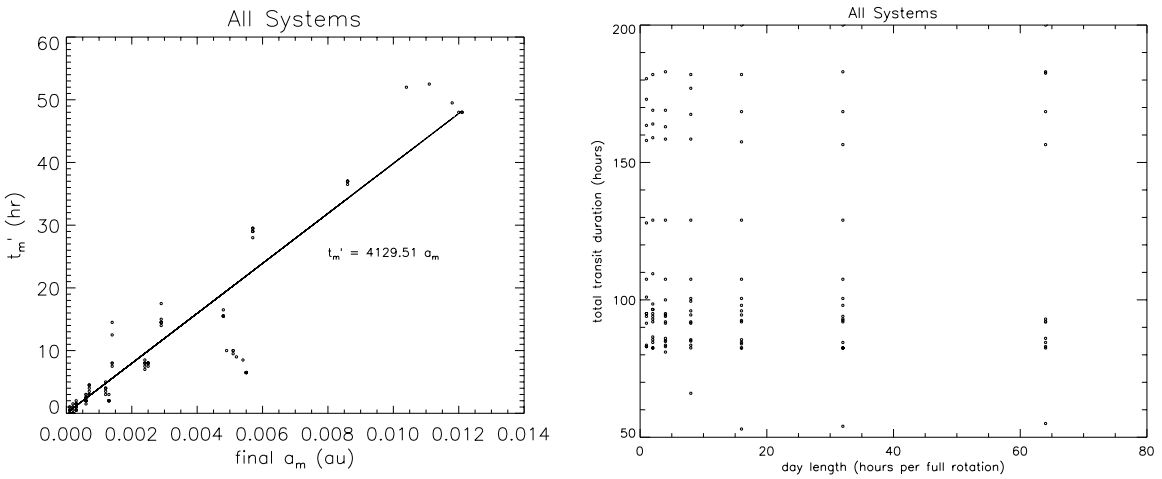

(a) (b)

Figure 3.1: (a) shows the moon's independent transit duration, t'_m, for all configurations as a function of the moon's final semi-major axis, a_m after each five year integration (125 data points shown). Linear regress shown on plot. Recall that all integrations represent the optimal case of a planet and moon in noninclined, noneccentric orbits and an observer that is perfectly aligned with the eccliptic plane. While the numerical relationship leaves a lot to be desired, it logically makes sense the larger the separation between the planet and the satellite, the longer the overall duration of moon-transit. (b) shows the sum of all transits; planet, moon, and mutual; as a function of the rotation rate of the planet. Notice the total transit duration marginally decreases in range as the planet rotates faster. I suspect this trend merely exists as a result of fast rotating planet's tendency to eject close-in moons from orbit, thus the relevant datum were discarded.

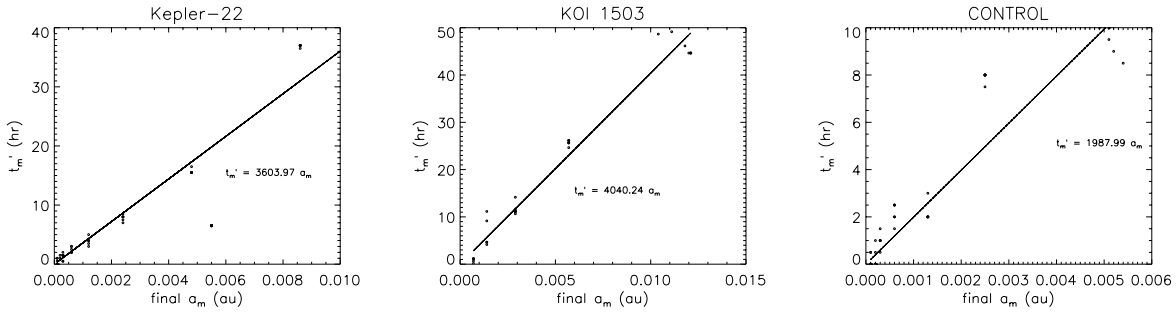

(a) (b) (c)

Figure 3.2: (a), (b), and (c) show sufficient linear fits for t'_m as a function of the moon's semi-major axis, a_m. This is largely a sanity check, as the more separated the moon's signal is from the planet's signal, the more likely they are independently detectable. .

Now, holding the semi-major axis constant across every row, I investigate the effect of planetary spin on transit data. In the following examples, the moon's radius is amplified to $R_p/2$ to magnify its signal during transit.

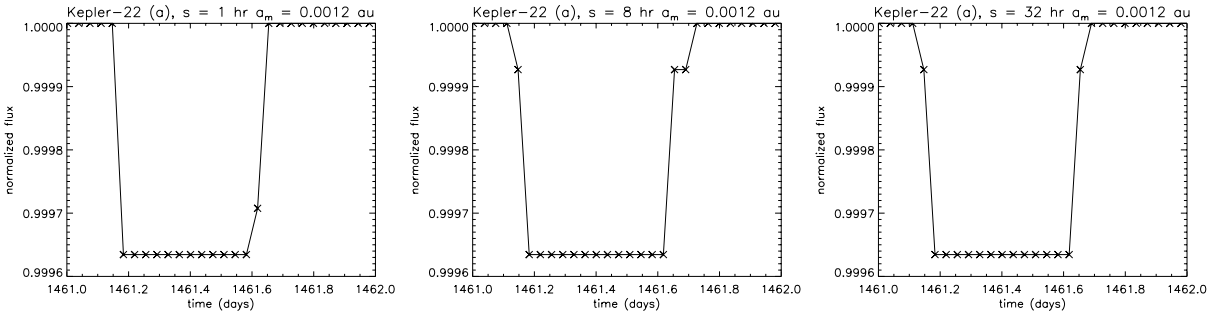

(a) (b) (c)

Figure 3.3: This Kepler-22 configuration has an extremely close-in moon at $r_H/16$, which thus experiences significant tidal torque from the primary. The moon's signal is indistinguishable from the primary's in the fast-rotator trial, (a). In slow-rotators (b) and (c), the moon peeks out during the ingress and egress of the transit, but for the most part its signal is barely visible.

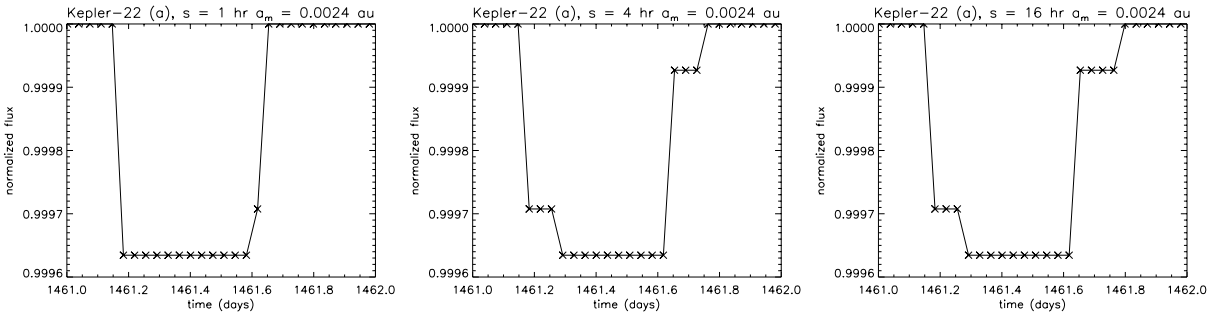

(a) (b) (c)

Figure 3.4: This Kepler-22 configuration with a moderately detectable moon at $r_H/4$ shows significant change at rotation rates < 4 hours/rotation.

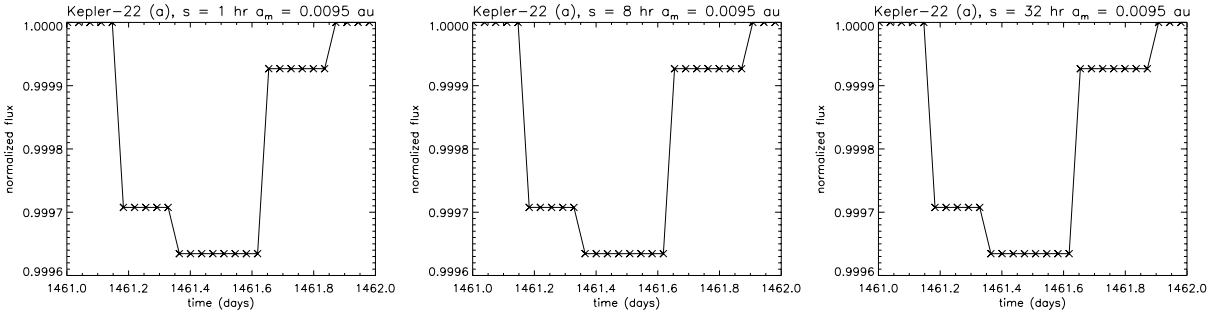

(a) (b) (c)

Figure 3.5: This Kepler-22 configuration shows no sign of spin rate affecting the light curve. The moon in this case fringes at $r_H/2$, so it likely does not experience enough torque from the rotator to affect its orbit.

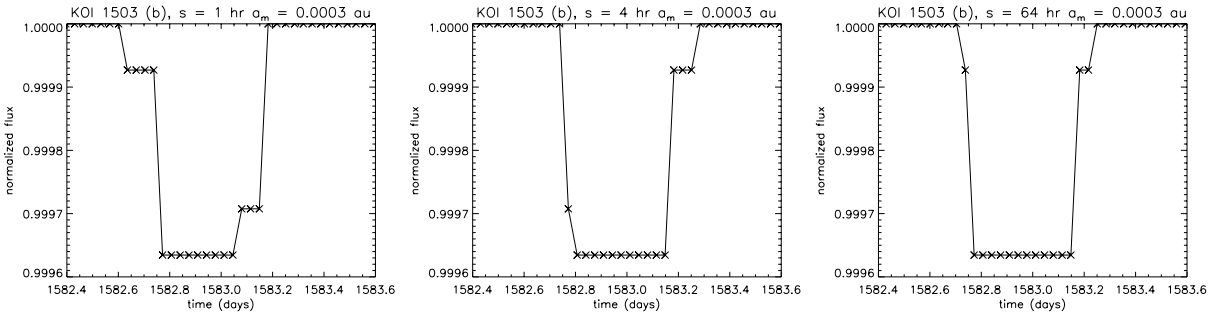

(a) (b) (c)

Figure 3.6: This KOI 1503 configuration has an extremely close-in moon, at $r_H/16$, which is significantly affected by planetary spin. In the fast rotator, the moon's independent signal appears to manifest itself during transit far more than in the slower cases. Recall KOI 1503 is the most massive and close-in planet, so its spin rate should affect the moon's orbit the most significantly out of the three configurations.

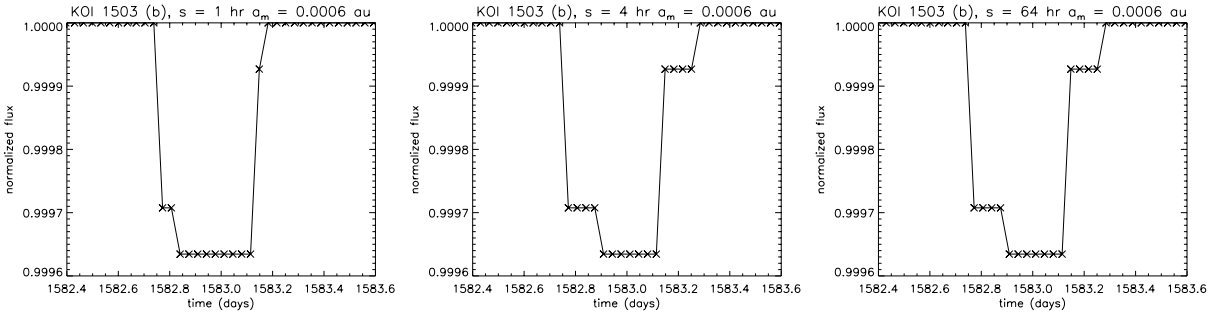

(a) (b) (c)

Figure 3.7: At the moderate semi-major axis shown, $r_H/4$, the spin rate significantly affects the light curve at rates greater than 4 hours/rotation.

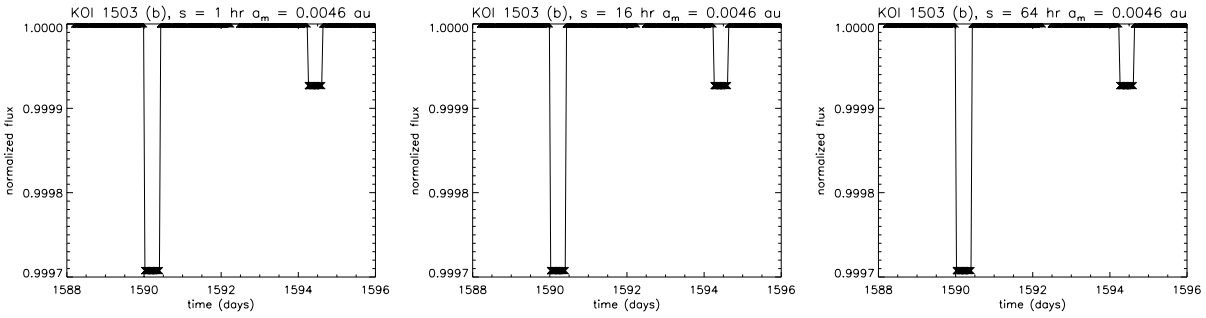

(a) (b) (c)

Figure 3.8: The moon at $r_H/2$ in this configuration appears not to be significantly affected by the planet's rotation rate.

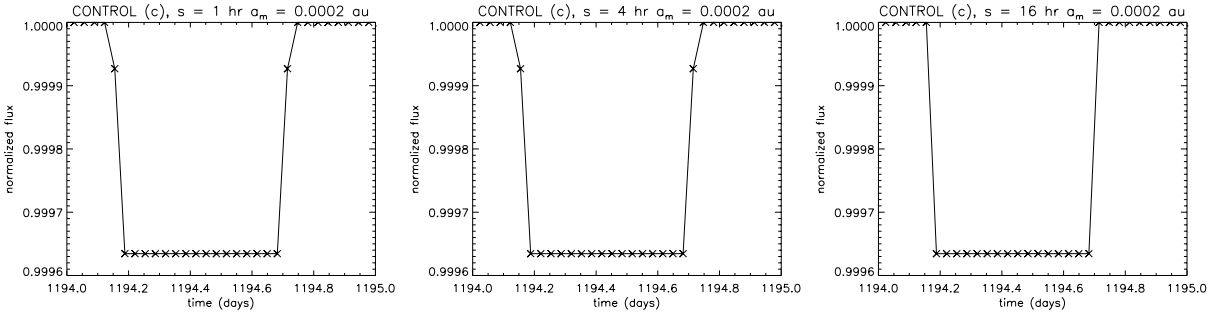

(a) (b) (c)

Figure 3.9: The close-in moon, $r_H/16$, for the Control system shows the moon signal becomes less differentiable from the primary as the rotation slows down. This demonstrates how sensitive t'_m is to the system's parameters, as the opposite effect is observable in Figure (3.3).

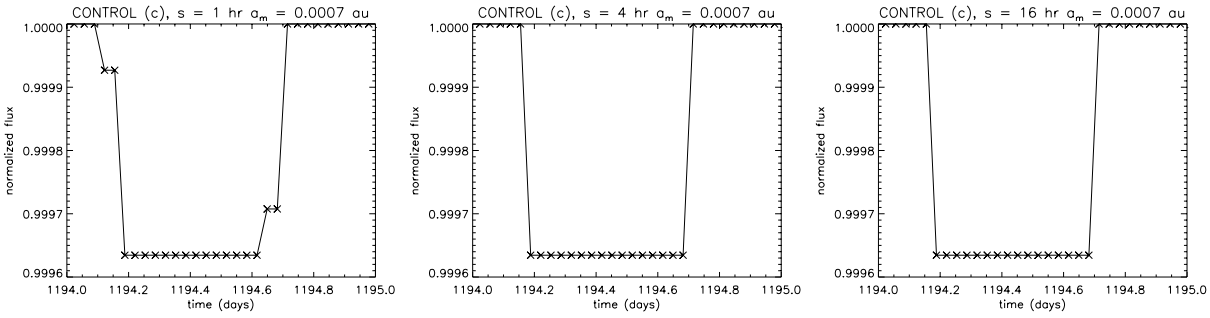

(a) (b) (c)

Figure 3.10: At this semi-major axis, $r_H/8$ the light curve is only affected at rotation rates greater than 4 hours/rotation.

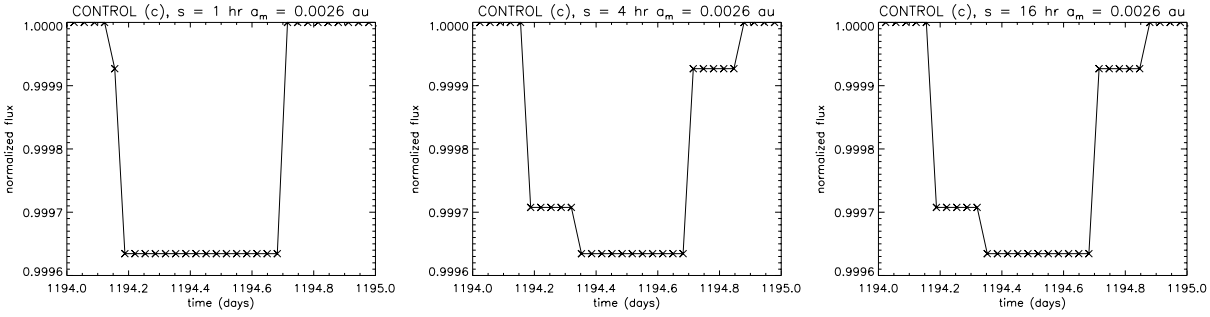

(a) (b) (c)

Figure 3.11: Surprisingly a small effect is observable in the photometry with a moon at $r_H/4$. This is interpreted as a possible cut-off point in which the rotation rate stops affecting photometry data for planets with densities ($\geq$ 5.5 g/cc).

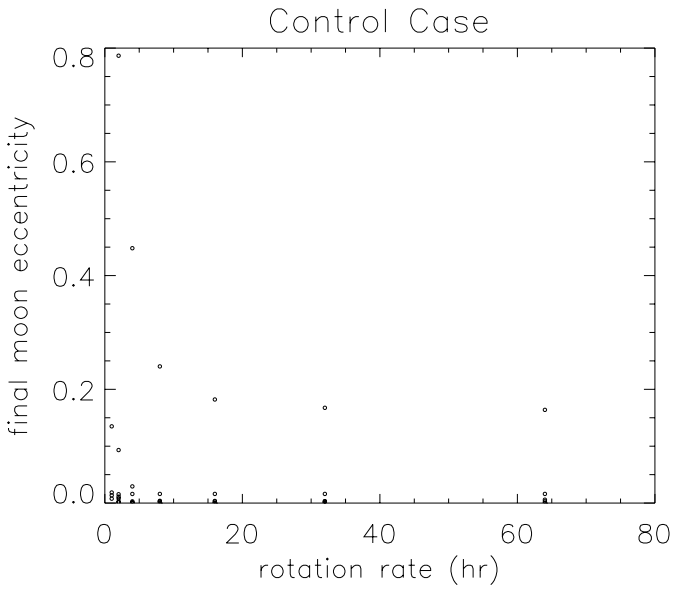

Figure 3.12: Control configuration: comparison of the final eccentricity of the moon as a function of the rotation rate of the planet.

3.1 Interpretation

There is no detectable change in the light curve when the moon is sufficiently far away, as shown in Figures 3.5 and 3.8 which incorporate a moon > 0.004 au; the cut off point at which axial rotation stops affecting the photometry is $\approx r_H/4$ for the five year time span. At sufficiently small a_m, I observe the transiting moon tends to significantly change the light curve as a function of spin rate.

Quantifying this effect, however, is not so clear-cut.

I suspect a faster rotation rate increases the moon's eccentricity significantly over the five year run. For all configurations, the initial zero eccentricity increased to 0.05, on average, by the five year mark. There is an indication of a correlation, shown in Figure 3.12, between fast rotators

and high eccentricities for the Control configuration. The other systems (not shown) show a less clear trend, but the mechanism which increases eccentricity significantly is clearly expressing itself in the light curves.

Alternatively, a depression of the moon's semi-major axis should cause a decrease in t'_m, according to Figure 3.1 (a). To check if the moon's semi-major axis lowers significantly over the five year time span, the semi-major axes of a fast rotator's moon and a slow rotator's moon are overlain. However, as shown in Figure 3.13, the exact opposite is true! During transit, the moon actually has a larger semi-major axis during the fast-rotation case.

Therefore, the coupling between planetary spin and the moon's orbital parameters – eccentricity, semi-major axis, etc – make the planetary rotation rate indeterminable without precise knowledge of how these affect the shape of the light curve.

3.2 Conclusion

Overall, the results indicate that planetary spin only becomes relevant in photometry at low moon semi-major axes, wherein $a_m < r_H/4$. Unfortunately, in such configurations the planet and moon signals are not easily differentiable. Additionally, the significant "pumping up" of the moon's eccentricity appears to be confounding the results, as this parameter was not controlled for.

One weakness of the experiments performed is the lack of numerical simulations. The area between the Hill radius and Roche limit represent but one plane within a greater sphere of

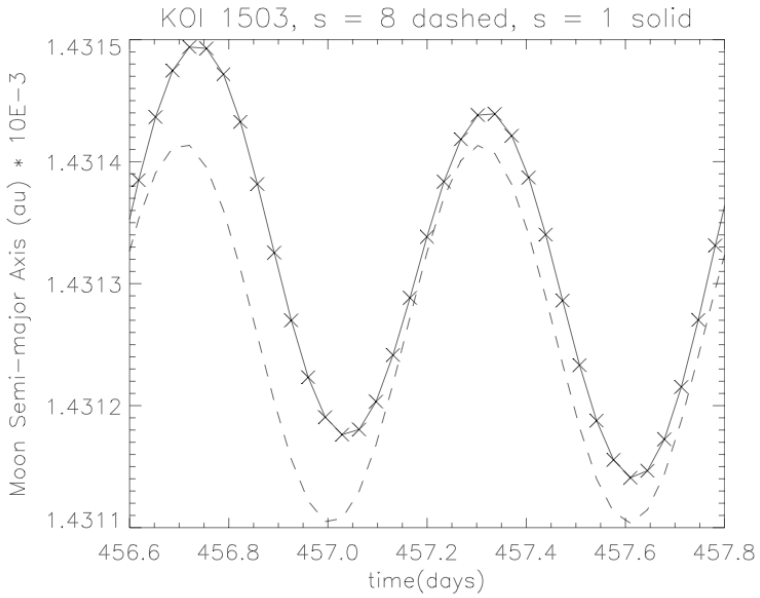

Figure 3.13: KOI 1503 configuration; a comparison of the fast rotator's moon semi-major axis (solid) with the slow rotator's moon semi-major axis (dashed) during transit. It is more difficult to differentiate the moon's signal from the planet's in the fast rotator's light curve, so I expect it should have a lower semi-major axis. The opposite, however, seems to be the case.

moon-hosting probability. While the case where the moon is maximally separated from its host planet represents the highest probability of distinguishing its signal, moons can, and do, exist at any arbitrary area in the Hill sphere. Additionally, the mass and interior parameters of the moon and planet are poorly constrained, so more leeway in these parameters may produce realistic results. Also, this paper only analyzes box-plot transit light curves, which do not take into account stellar limb darkening and other important spectral features. Future studies into this subject would benefit from using sophisticated Mandel and Agol (2002) light curve routines when producing fits to real data.

Natural satellites may be the key to finding the first true Earth analogue in an extrasolar-system. The sheer quantity of natural satellites in our solar system motivate the search for moons elsewhere. The discovery of an exomoon in transit may allow one to infer the primary's spin rate, but further research into this subject must be done.

Bibliography

Barnes, J. W. and D. P. O'Brien (2002, August). Stability of Satellites around Close-in Extrasolar Giant Planets. *575*, 1087–1093.

Batalha, N. M., J. F. Rowe, S. T. Bryson, T. Barclay, C. J. Burke, D. A. Caldwell, J. L. Christiansen, F. Mullally, S. E. Thompson, T. M. Brown, A. K. Dupree, D. C. Fabrycky, E. B. Ford, J. J. Fortney, R. L. Gilliland, H. Isaacson, D. W. Latham, G. W. Marcy, S. Quinn, D. Ragozzine, A. Shporer, W. J. Borucki, D. R. Ciardi, T. N. Gautier, III, M. R. Haas, J. M. Jenkins, D. G. Koch, J. J. Lissauer, W. Rapin, G. S. Basri, A. P. Boss, L. A. Buchhave, D. Charbonneau, J. Christensen-Dalsgaard, B. D. Clarke, W. D. Cochran, B.-O. Demory, E. Devore, G. A. Esquerdo, M. Everett, F. Fressin, J. C. Geary, F. R. Girouard, A. Gould, J. R. Hall, M. J. Holman, A. W. Howard, S. B. Howell, K. A. Ibrahim, K. Kinemuchi, H. Kjeldsen, T. C. Klaus, J. Li, P. W. Lucas, R. L. Morris, A. Prsa, E. Quintana, D. T. Sanderfer, D. Sasselov, S. E. Seader, J. C. Smith, J. H. Steffen, M. Still, M. C. Stumpe, J. C. Tarter, P. Tenenbaum, G. Torres, J. D. Twicken, K. Uddin, J. Van Cleve, L. Walkowicz, and W. F. Welsh (2012, February). Planetary Candidates Observed by Kepler, III: Analysis of the First 16 Months of Data. *ArXiv e-prints*.

Borucki, W. J., D. G. Koch, N. Batalha, S. T. Bryson, J. Rowe, F. Fressin, G. Torres, D. A. Caldwell, J. Christensen-Dalsgaard, W. D. Cochran, E. DeVore, T. N. Gautier, J. C. Geary, R. Gilliland, A. Gould, S. B. Howell, J. M. Jenkins, D. W. Latham, J. J. Lissauer, G. W. Marcy, D. Sasselov, A. Boss, D. Charbonneau, D. Ciardi, L. Kaltenegger, L. Doyle, A. K. Dupree, E. B. Ford, J. Fortney, M. J. Holman, J. H. Steffen, F. Mullally, M. Still, J. Tarter, S. Ballard, L. A. Buchhave, J. Carter, J. L. Christiansen, B.-O. Demory, J.-M. Desert, C. Dressing, M. Endl, D. Fabrycky, D. Fischer, M. R. Haas, C. Henze, E. Horch, A. W. Howard, H. Isaacson, H. Kjeldsen, J. A. Johnson, and T. Klaus (2012, February). Kepler-22b: A 2.4 Earth-radius Planet in the Habitable Zone of a Sun-like Star. *The Astrophysical Journal 745*, 120.

Domingos, R. C., O. C. Winter, and T. Yokoyama (2006, December). Stable satellites around extrasolar giant planets. *Monthly Notices of the Royal Astronomical Society 373*, 1227–1234.

Kipping, D. M. (2011, September). LUNA: an algorithm for generating dynamic planet-moon transits. *Monthly Notices of the Royal Astronomical Society 416*, 689–709.

Kipping, D. M. (2012, January). The Hunt for Exomoons with Kepler. In *American Astronomical Society Meeting Abstracts*, Volume 219 of *American Astronomical Society Meeting Abstracts*, pp. 414.05.

Mandel, K. and E. Agol (2002, December). Analytic Light Curves for Planetary Transit Searches. *The Astrophysical Journal 580*, L171–L175.

Mardling, R. A. and D. N. C. Lin (2002, July). Calculating the Tidal, Spin, and Dynamical Evolution of Extrasolar Planetary Systems. *The Astrophysical Journal 573*, 829–844.

Murray, C. D. and S. F. Dermott (1999). *Solar system dynamics*.

Press, W. H., B. P. Flannery, and S. A. Teukolsky (1986). *Numerical recipes. The art of scientific computing*.

Simon, A. E., G. M. Szabó, K. Szatmáry, and L. L. Kiss (2010, August). Methods for exomoon characterization: combining transit photometry and the Rossiter-McLaughlin effect. *Monthly Notices of the Royal Astronomical Society 406*, 2038–2046.

Valencia, D., R. J. O'Connell, and D. Sasselov (2006, April). Internal structure of massive terrestrial planets. *Icarus 181*, 545–554.

Weidner, C. and K. Horne (2010, October). Limits on the orbits and masses of moons around currently-known transiting exoplanets. *aap 521*, A76.